Parameters controlling fracture resistance in functionally graded materials under mode I loading

Jorge Abanto-Bueno [1], John Lambros [*]

Department of Aerospace Engineering, University of Illinois at Urbana-Champaign, Urbana, IL 61801, USA

Abstract

In this investigation the fracture behavior of functionally graded materials (FGMs) was studied by means of experiments carried out on model polymer-based FGMs. Model graded materials were manufactured by selective ultraviolet irradiation of ECO [poly(ethylene carbon monoxide)], a photo-sensitive ductile copolymer that becomes more brittle and stiffer under exposure to ultraviolet light. The mechanical response of the graded material was characterized using uniaxial tensile tests. Single edge notched tension graded ECO specimens possessing different spatial variations of Young's modulus, failure stress and failure strain were tested under remote opening loading. A full-field digital image correlation technique was used to measure in real-time the displacement field around the crack tip while it propagated through the graded material. The measured displacement field was then used to extract fracture parameters such as stress intensity factor and T-stress, and thus construct resistance curves for crack growth in the FGMs. For this loading configuration it was found that the nonsingular T-stress term in the asymptotic expansion for stresses needs to be accounted for in order to accurately measure the fracture resistance in FGMs. In addition, the influence of local failure properties (i.e., failure stress and failure strain) on crack growth resistance was investigated in detail. It was found that depending on the combined effects of the spatial variation of these two failure parameters, regardless of the spatial variation of the Young's modulus, the FGM fracture resistance can either increase, decrease or remain constant with continued crack growth.
© 2005 Elsevier Ltd. All rights reserved.

Keywords: Functionally graded materials; Crack growth resistance; Digital image correlation; T-stress; Poly(ethylene carbon monoxide)

---

[*] Corresponding author. Tel.: +1 217 333 2242; fax: +1 217 244 0720.
  E-mail address: lambros@uiuc.edu (J. Lambros).
[1] Present address: Department of Mechanical Engineering, Bradley University, Peoria, IL 61625, USA.

1. Introduction

Functionally graded materials (FGMs) are heterogeneous materials possessing thermomechanical properties that vary spatially in a continuous manner. Generally, these are ceramic/metal graded mixtures that exploit the beneficial properties of both metals (toughness, thermal conductivity, ductility, etc.) and ceramics (hardness, heat and corrosion resistance, etc.), while enhancing bond strength and reducing residual stresses when compared to metal/ceramic interfaces. FGMs were initially conceived as thermal protections systems for aerospace applications (Niino and Maeda, 1990), but are also being considered in applications such as energy conversion (Gasik and Ueda, 1999), military (Chin, 1999), microelectronics (Yamada et al., 1999), biomedical (Watari et al., 1999; Pompe et al., 2003) and machining (Zhao et al., 2002). However a better understanding of FGMs, especially regarding their fracture response, is needed to allow wider use of such materials.

There have been several analytical and numerical investigations that have shown that the asymptotic deformation fields around a stationary crack in an FGM with continuous and piecewise differentiable property variation are identical to those in homogeneous materials with properties evaluated at the crack tip location (Eischen, 1987; Parameswaran and Shukla, 2002; Chalivendra et al., 2003; Kubair et al., 2005). Other studies have determined stress intensity factors in cracked linear elastic FGMs (Delale and Erdogan, 1983; Konda and Erdogan, 1994; Erdogan and Wu, 1997; Anlas et al., 2000; Kim and Paulino, 2003). However, equally important in the characterization of FGMs is to understand the mechanisms and material parameters that control crack *propagation* in these heterogeneous materials.

For homogeneous materials under small scale yielding conditions quasi-static crack growth is governed by a resistance curve which is a material property that depends on crack extension (Anderson, 1995). Such a crack growth criterion can be expressed mathematically as

$$K_I(P, a) = K_I^R(\Delta a), \tag{1}$$

where K_I is the current crack tip stress intensity factor, generally a function of applied load (P) and geometry (a), and K_I^R is a material property representing crack growth resistance and is a function of crack extension only (Δa). To date there have been very few studies of crack *growth* in graded materials and it is not known in detail how Eq. (1) can be applied for FGMs. One of the goals of the present work is to evaluate the applicability of Eq. (1) to quasi-static crack growth in FGMs.

One of the first attempts at modeling crack propagation in an FGM was performed by Jin and Batra (1996), who considered a metal particulate reinforced ceramic composite with graded composition. Crack growth resistance curves (R-curves) for the FGM were predicted using two models, the rule of mixtures and a linear crack bridging law (crack bridging stress, σ, prescribed as a function of crack opening displacement, δ, on the cohesive zone just ahead of the crack tip). Both models predicted an increase in fracture resistance, referred to as "built-in" toughening by Erdogan (1995), when the crack propagates from the ceramic-rich region to the metal-rich one. However the trend followed by the two calculated R-curves differs, as shown schematically in Fig. 1. Clearly which of the two responses will dominate depends on the micromechanical mechanisms present in each case and can be answered through experimentation.

Experimental work on the fracture of FGMs is, however, still lacking when comparing to theoretical efforts. Butcher et al. (1999) used a gravity casting technique to generate a graded particulate composite having varying volume fraction of spherical glass particles in a polymer matrix. They used the optical technique of reflection coherent gradient sensing (CGS) to determine the critical stress intensity factor for crack initiation of an edge crack positioned at the interface between the FGM and a homogeneous material. Rousseau and Tippur (2000) extended the work of Butcher et al. (1999) and determined critical stress intensity factors for crack initiation for an edge crack situated at different locations along the graded region, but always perpendicular to the material stiffness gradient. Li et al. (2000) used a hybrid numerical–experimental approach to generate for the first time a crack growth resistance curve for a polymer-based functionally
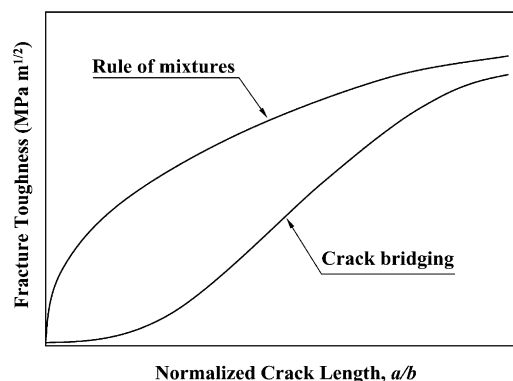
Fig. 1. Schematic representation of the two possible crack growth resistance curves calculated by Jin and Batra (1996) using the concepts of rule of mixtures and crack bridging for a theoretical metal reinforced ceramic matrix composite.

graded material manufactured from a photo-sensitive polyethylene copolymer using the technique developed by Lambros et al. (1999). Li et al. (2000) observed that the FGM exhibited a significant "built-in" resistance curve as the crack grew from the stiffer region to the more complaint one resembling the fracture resistance curve calculated by Jin and Batra (1996) using a crack bridging law (see Fig. 1). Abanto-Bueno and Lambros (2002) generated similar crack growth resistance curves for model polymer-based FGMs from experimental measurements of near crack tip displacement fields using the full-field digital image correlation technique. More recently, Neubrand et al. (2003) have found a monotonically increasing R-curve for graded Al/Al_2O_3 composites possessing a graded region of 17.5 mm and prepared using an adaptation of the foam replication process first described by Cichocki et al. (1998). They have also shown that the gradient in elastic properties of the FGMs directly affects the crack driving force for crack propagation.

Most of the above mentioned studies have either dealt with stationary cracks or have demonstrated the "built-in" resistance curve of the graded material for very specific FGM property gradients. The goal of the present work is a more detailed experimental analysis in which the role of both local elastic and local failure properties is investigated in depth. As can be concluded from the work of Jin and Batra (1996) different models, which are related to potentially different local properties and/or failure mechanisms, can significantly affect the response of the graded material. In this work we will exploit the flexibility of the specimen preparation technique described by Lambros et al. (1999) to generate a series of FGMs with markedly different property variation. Special emphasis is also placed on making full-field optical measurements around the growing crack tip (loaded in mode I) so that an accurate measure of the crack growth resistance can be obtained. In addition, care is taken to have a precise knowledge of the variation of mechanical and failure properties in each FGM tested. Details of the manufacturing process of model FGMs and the experimentation procedure are given in Section 2. In Section 3 the results and discussion of the mechanical and fracture characterization are presented in detail and conclusions are drawn in Section 4.

2. Experimental procedure and methodology

2.1. Fabrication of model FGMs

The technique initially developed by Lambros et al. (1999) to manufacture model polymer-based functionally graded materials from photo-sensitive poly(ethylene carbon monoxide), ECO, was also used in this investigation. However, since here we are interested in detailed knowledge of both elastic and failure

property variation, a more reliable fabrication procedure and a more comprehensive mechanical properties characterization protocol was employed. Only the improvements made are described below and the reader is referred to Lambros et al. (1999) for more details on the technique.

The basic idea behind the technique developed by Lambros et al. (1999) is to exploit the ductile-to-brittle transition that ECO exhibits upon ultraviolet (UV) light exposure (Andrady, 1990; Abanto-Bueno and Lambros, 2004) to generate graded materials. The transition from shear yielding dominated (ductile) to craze dominated (brittle) failure, also confirmed through SEM microscopy (Ivanova et al., 1996; Lambros et al., 1999), produces a stiffer but more brittle material as UV irradiation of ECO increases. By gradually increasing the UV exposure time on thin ECO samples along their width, a continuous spatial transition from a ductile mechanical response (short irradiation periods) to a more brittle one (long irradiation times) is achieved. The major modification over the set-up of Lambros et al. (1999) is the use of a computer controlled motorized translation stage (Model M-415.DG, Polytec PI, Inc., Auburn, MA) allowing for three improvements: (i) a highly uniform translation speed, (ii) a very slow speed down to 0.15 mm/h (verified through calibration using a linear variable differential transformer, LVDT), and (iii) the capability to program in the computer a specific sequence of varying speeds in order to generate different gradients and/or steps in mechanical properties. Furthermore, by translating the ECO samples in front of the stationary UV source, as opposed to using a moving shield as in Lambros et al. (1999), two samples which have the same in-plane property variation can be manufactured simultaneously. Using this modified technique, in-plane graded FGM samples having dimensions up to 300 mm × 170 mm were manufactured. The UV irradiation time, and thus the material property, of every sample is uniform along its length (300 mm) and decreases (or increases) continuously along its entire width (170 mm), or a fraction of it, depending on the desired mechanical property variation. The thickness of each sample is small enough (0.406 mm) to ensure homogeneous irradiation through the thickness.

Because of their relevance to the present work four different and representative FGMs are presented in detail here. They have been labeled as FGM I, II, III and IV. The initial nominal dimensions of samples FGM I and II were 300 mm × 150 mm, and of FGM III and IV were 300 mm × 170 mm. FGM I and II were first homogeneously irradiated for 5 h over their entire area. Then for the case of FGM I, its entire width (150 mm) was graded by moving the translation stage at 0.77 mm/h for 195 h; while for the case of FGM II a graded region of only 39 mm was generated by moving the translation stage speed of 0.20 mm/h for 195 h. In the case of FGM III and IV, their entire area (300 mm × 170 mm) was homogeneously irradiated for 1 h and then continuously irradiated for 200 h while moving the translation stage at a speed of 0.24 mm/h resulting in a total graded area of 300 mm × 48 mm. The graded region in FGM III and IV started at 25 mm and 35 mm from one of the ends, respectively.

2.2. Tensile testing

Irradiated ECO possesses significant variability in its mechanical properties (Andrady, 1990; Andrady et al., 1993; Ivanova et al., 1996; Abanto-Bueno and Lambros, 2004). Therefore, to allow an accurate correlation between the FGM fracture response and its local mechanical properties, the spatial property variation was measured for every FGM tested. Once the manufacturing process was finished (8–10 days), every FGM sample underwent two sets of experiments: (i) a series of uniaxial tensile tests to characterize local mechanical property variation, and (ii) a fracture test. To this end, each sample was cut in two identical halves parallel to the UV irradiation direction as illustrated in the left-hand side of Fig. 2. One half was used to generate a single edge notched tension fracture specimen, while the other half was cut into thin strips perpendicularly to the UV irradiation direction for uniaxial tensile testing. Fig. 2 shows the dimensions of a typical FGM sample (left-hand side), and the geometry and dimensions of the specimens obtained from it to perform both the uniaxial tensile tests and the fracture test (right-hand side).
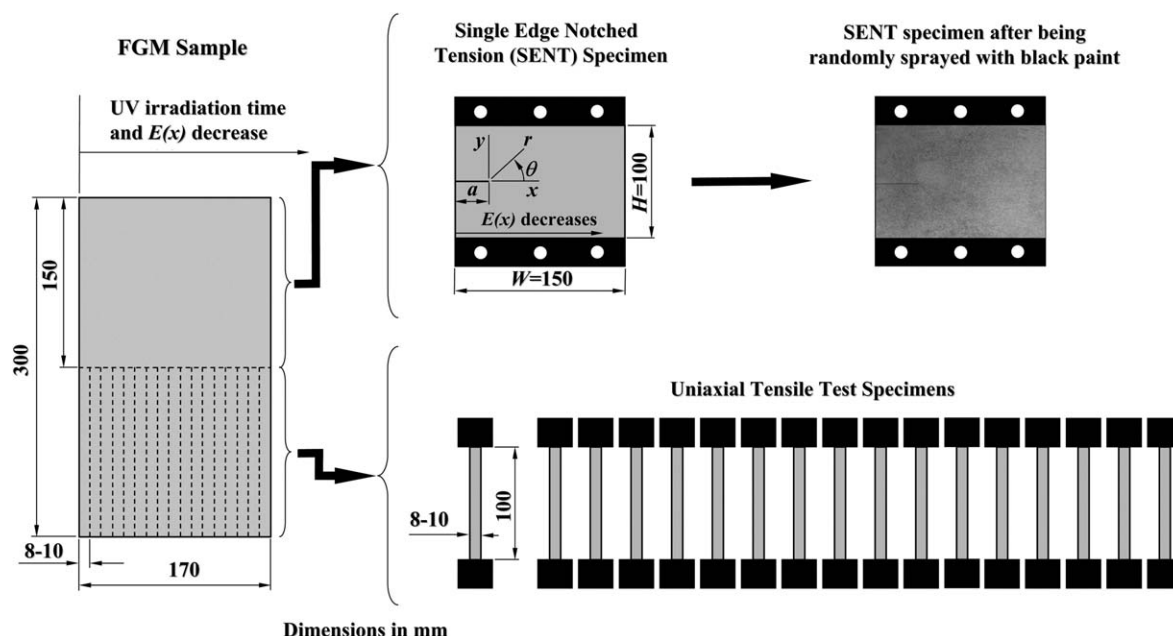
Fig. 2. Typical FGM sample (left) showing its dimensions, and the geometry and dimensions of the specimens used for its mechanical and fracture characterization (right). SENT specimen dimensions: a = crack length, W = specimen width and H = specimen length (thickness = 0.406 mm).

The uniaxial tension tests were carried out using a tabletop universal testing machine (Model Alliance RT/30, MTS Systems Comporation, Eden Prairie, MN) under displacement control conditions at a rate of 0.5 mm/min. A 100 lb load cell (Transducer techniques Inc., Temecula, CA) was used to measure the applied load. The universal testing software TestWorks® 4 (MTS Systems Corporation) was used to control the testing machine and to acquire the instantaneous machine crosshead displacement and corresponding applied load data. This software was also used to measure the material Young's modulus.

2.3. Fracture testing

Single edge notched tension (SENT) fracture specimens, originating from the same sample on which the tensile testing was conducted, were tested to failure on the MTS RT/30 machine under displacement control conditions. Using a sharp razor blade, a 30 mm through thickness sharp pre-crack, having approximately 1.5 μm radius of curvature, was placed parallel to the gradient direction in the stiffer side of the FGM specimen. The same loading rate as in the uniaxial tension tests (0.5 mm/min) was used so that any rate dependence effects would be minimized and a direct comparison between tensile and fracture responses could be made. Specimen gripping was done through friction grips that were developed specifically for this material and loading configuration during an earlier study (Lambros et al., 1999). A uniform displacement along the upper grip was applied in the positive y-direction, while the lower grip was held fixed. Applied displacement and resulting load signals were recorded (see Fig. 2 for axes definition). Since both the applied loading was symmetric and the initial crack was parallel to the material property gradient Mode I conditions prevailed throughout the test, and the crack grew straight ahead along the initial crack line. Fig. 3 shows a photograph of the crack path followed for a typical mode I FGM fracture test.
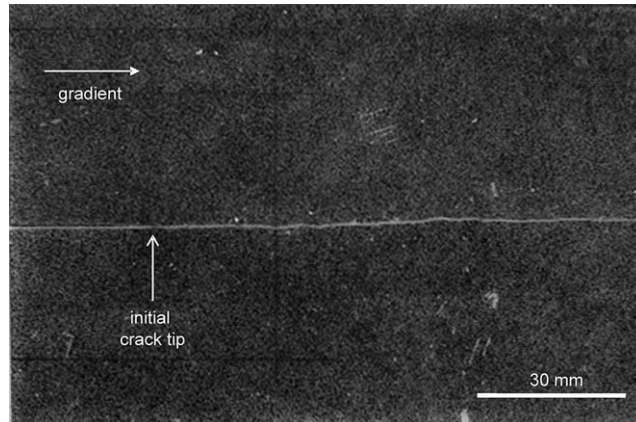
Fig. 3. Photograph showing typical crack path in FGM SENT fracture specimen.

Prior to fracture testing one surface of the specimen was sprayed with black paint using an airbrush to create a random speckle pattern which is needed to measure the in-plane surface deformation using the full-field optical technique of digital image correlation (DIC). An IEEE 1394 digital CCD camera (Sony XCD-SX900, 1280 × 960 pixels resolution) was focused at the region around the crack tip and was used to record the speckle pattern, at a rate of 0.5 frames per second, during the crack initiation and growth event. Fig. 4 shows two typical digital pictures corresponding to times before crack initiation (Fig. 4(a)) and during crack growth (Fig. 4(b)). The speckle pattern on the surface, used in the DIC technique to track in-plane surface displacement, is clearly visible. For completeness, a brief description of the DIC technique is given in the next section.

2.4. Digital image correlation technique

Digital image correlation (DIC) is a robust technique used to accurately measure full-field deformations (displacement and strain) by comparing the local features of a pair of digital images of a random speckled surface of a body taken before and after deformation. Details of the method can be found in the literature (Sutton et al., 1983; Bruck et al., 1989; Vendroux and Knauss, 1998) and will not be discussed here. The difference of the technique used in this study with that used in other efforts centers around the execution of the DIC algorithm. In this investigation, a hybrid DIC scheme having three consecutives steps, which combine the two most accepted DIC minimization methods available in the literature, the Coarse–fine (Sutton et al., 1983) and Newton–Raphson (Bruck et al., 1989) methods, was implemented. The first step is a variant of the Coarse–fine method and gives an approximate measurement of the displacement field by neglecting displacement gradients. In the second step, an approximate strain field is determined by numerically differentiating the displacement field obtained in step one. In the third step, the Newton–Raphson approach is used to compute the actual displacement and strain fields using as initial conditions the approximate displacement and strain fields obtained from steps one and two, respectively. Using this approach computational time is considerably reduced over the traditional DIC Coarse–fine technique without losing accuracy, which is ensured by using the Newton–Raphson approach in the third step.

The speckle pattern, generated using an airbrush, contained a distribution of speckles with an average size of 10 μm, or about 0.13 pixels for the average image resolution of 13 pixels/mm used here. This speckle pattern was seen in earlier work to correlate well for the SENT fracture experiments (Abanto-Bueno and
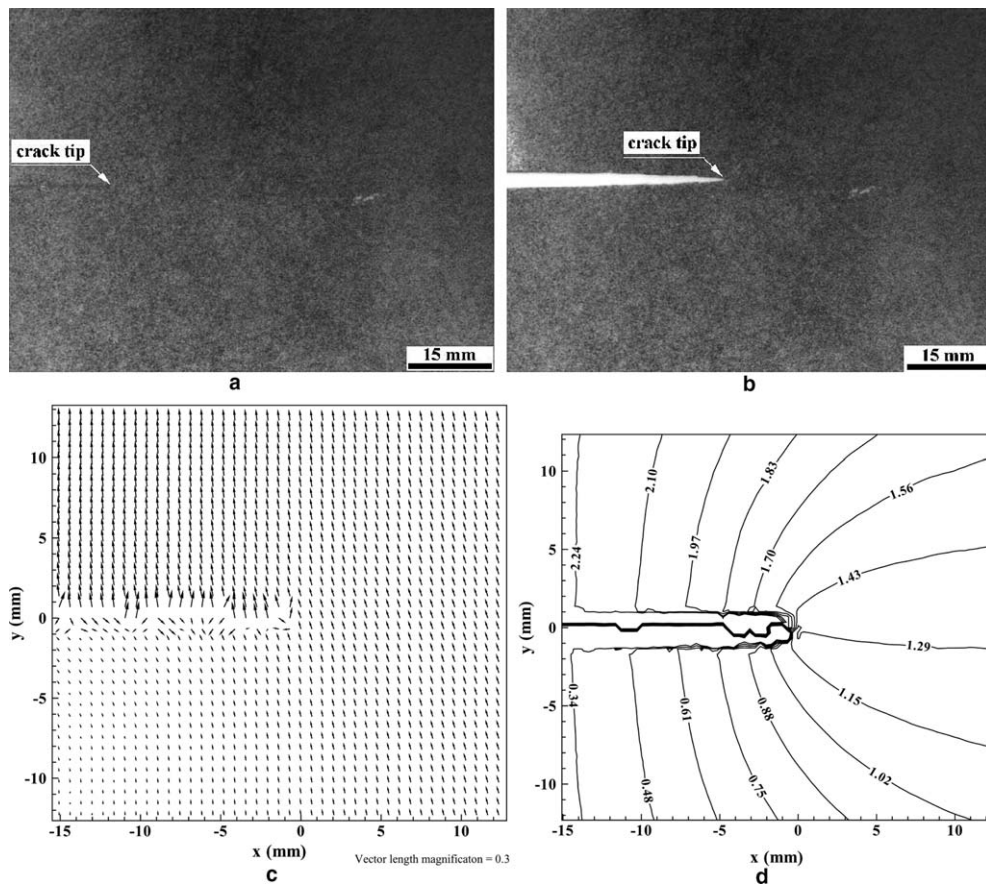
Fig. 4. DIC technique used in the deformation measurements of a SENT specimen: (a) undeformed state, (b) deformed state, (c) vector plot of the measured in-plane displacement field for the instant shown in (b), and(d) contours of the dominant displacement component for the configuration used (i.e., in the *y*-direction). In (c) and (d) the *x*-axis is parallel to the crack line and the crack tip is located at the origin.

Lambros, 2004). In all cases correlation was performed on a subset size of 31×31 pixels with a spacing between correlated subsets of 10 pixels. With the resolution used here this produces a displacement field at 6561 (81×81) correlation points over about a 62×62 mm field of view. An in-house code was developed to perform the correlation process.

Typical images that where collected during a fracture experiment and the corresponding DIC measurements are shown in Fig. 4. Fig. 4(a) is a snapshot of the region of interest before deformation, Fig. 4(b) is an image of a deformed configuration (notice that the crack has grown), Fig. 4(c) is a vector plot of the measured in-plane displacement field for the instant shown in Fig. 4(b) and Fig. 4(d) shows contours of the *y*-displacement component. In Fig. 4(c) and (d) the *x*-axis is parallel to the crack line and the crack tip is located at the coordinate origin. Of the 6561 points for which the correlation was performed only 1681 (41×41) are shown in Fig. 4(c), with the displacement vector plotted with 0.3 magnification. The contours in Fig. 4(d) use all the points of the correlation and no smoothing, other than the performed by the plotting program, has been done. The full-field information obtained is clearly visible. Analysis of these results is discussed in Section 3.2.

3. Results and discussion

3.1. Mechanical characterization of FGMs: Uniaxial tensile tests

Fig. 5(a)–(d) show five selected stress–strain curves (σ–ε) each from the uniaxial tensile tests (see Fig. 2) performed on FGM I, II, III and IV, respectively. To facilitate comparison between the four FGMs, the σ–ε curves have been plotted on the same scale. The individual σ–ε curves in Fig. 5 have been labeled by the center line position of the tension strip with respect to the stiffer end of the graded sample (i.e., the one exposed for longer UV irradiation times). As the irradiation time increases the material becomes stiffer in all the four cases, as was expected (Lambros et al., 1999). However in the case of FGM I, local failure strain, ε_f, and failure stress, σ_f, are independent of irradiation time remaining almost invariable (within experimental error) along the entire sample length (Fig. 4(a)). For the other three FGMs samples, two distinct regimes are observed: For longer irradiation times Young's modulus, E, and σ_f increase while ε_f
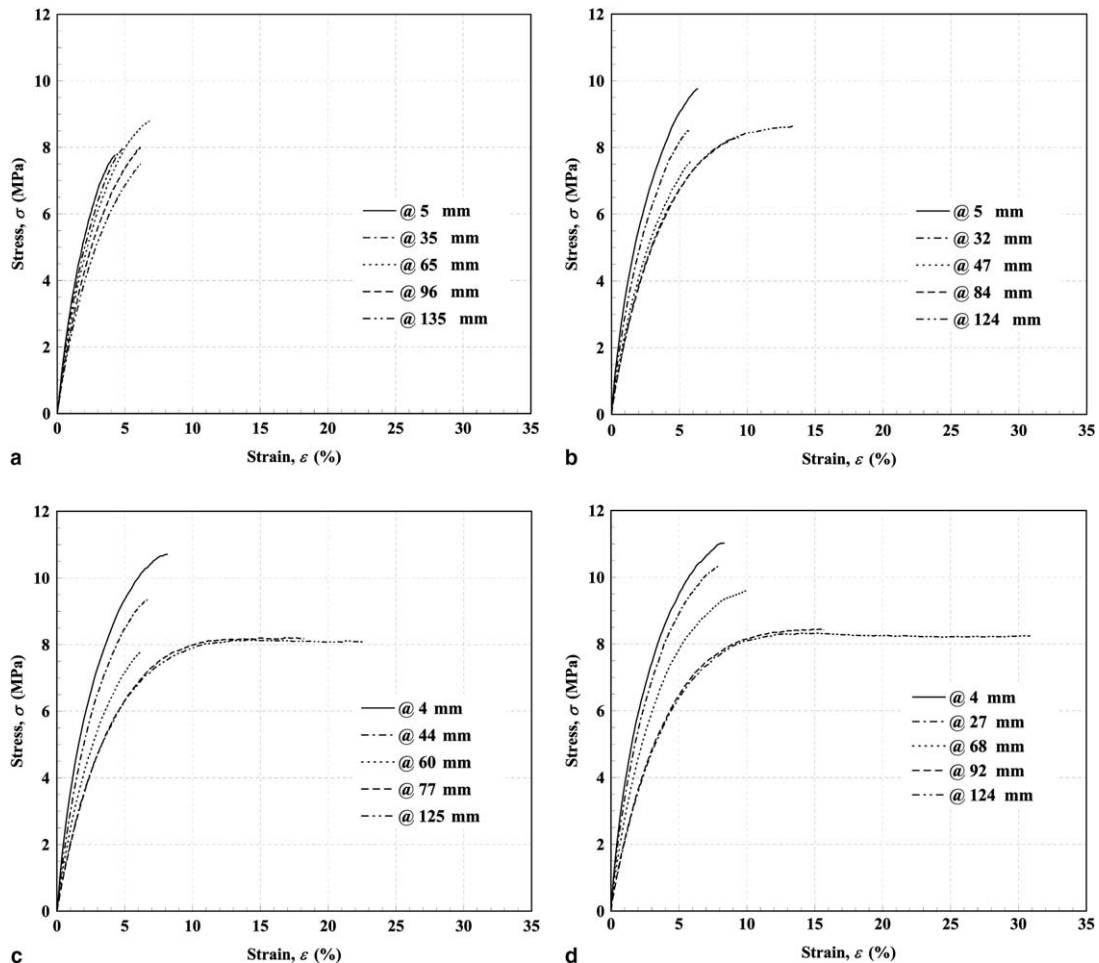

Fig. 5. Representative σ–ε curves for: (a) FGM I, (b) FGM II, (c) FGM III, and (d) FGM IV.

remains almost invariable, and for short irradiation times E and σ_f are approximately constant, while ε_f decreases considerably (Fig. 5(b)–(d)).

Plots of E, σ_f, and ε_f as a function of the FGM sample width have been constructed and are shown in Fig. 6(a)–(c), respectively. Recall that the width of the graded samples was either 150 mm (FGM I and II) or 170 mm (FGM III and IV). Young's modulus values for FGM I decrease continuously along the entire sample width from 350 MPa at one end to 230 MPa at the other end. FGM II possesses the property variation of an interphase in which three regions are observed: two homogeneous regions (20 mm and 90 mm wide) at each end, but with different Young's modulus, and a third region where E decreases in a continuous and smooth manner (as opposed to a sharp interface) between the two homogeneous regions. In this case, E decreases from 410 MPa to 235 MPa and the graded region width has been reduced to 38 mm resulting in a sharper Young's modulus transition. The spatial variation of E for FGM III and IV is similar and both possess only one homogeneous region after a graded portion. In both cases, E goes from 450 MPa to 205 MPa. Regarding the local failure properties of the FGMs, FGM I possesses almost constant failure stress, σ_f, ($\sim$8 MPa) and failure strain, ε_f, ($\sim$5.5%) along its entire width. In the case of FGM II, the behavior of σ_f is similar to the Young's modulus: constant at both ends but at different levels
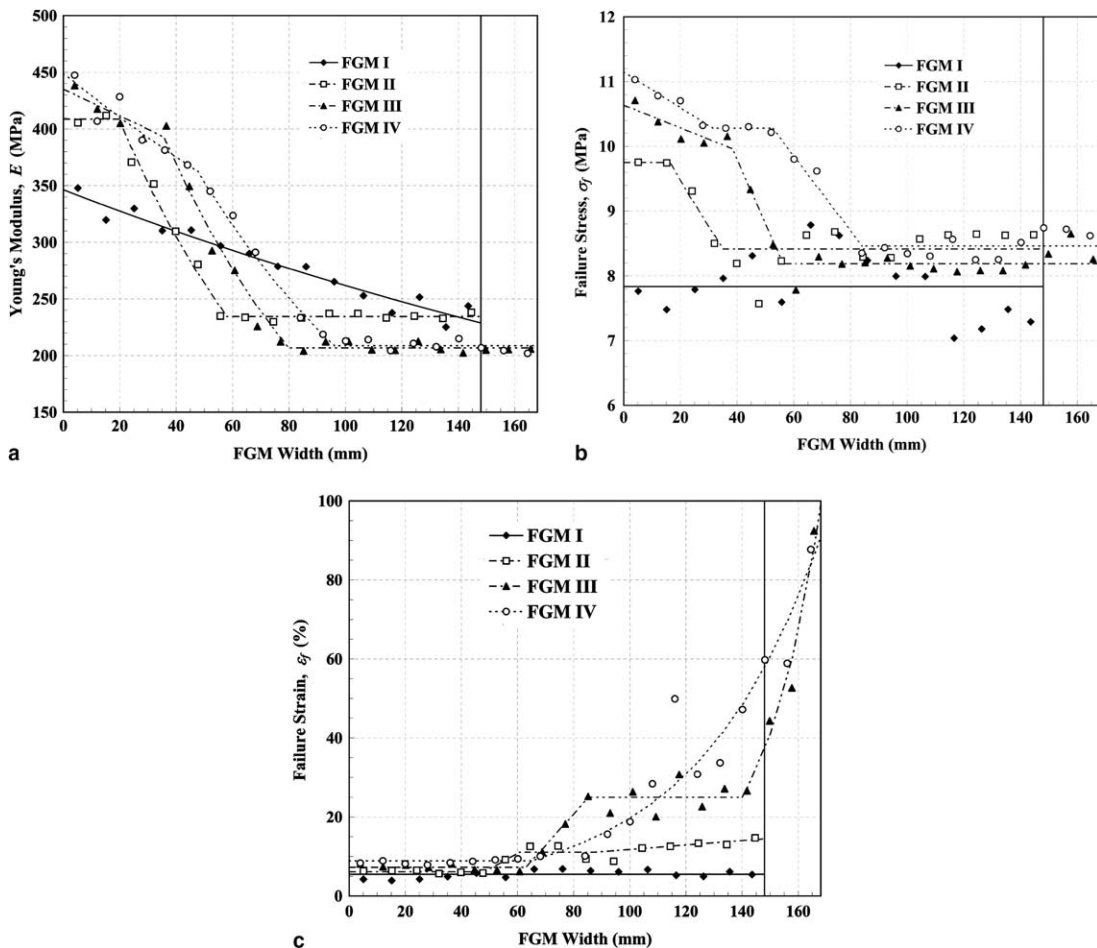

Fig. 6. Mechanical properties of FGMs I, II, III and IV as a function of their width: (a) Young's modulus, E, (b) Failure stress, σ_f and (c) Failure strain, ε_f. Data points are experimental measurements while solid lines represent the best fit to the measured data.

(9.75 MPa and 8.41 MPa) with an intermediate continuously decreasing graded region, while the failure strain has a constant value of 6% for the first 50 mm and then increases continuously up to 14% at the other end. The spatial variation of σ_f and ε_f are alike for FGM III and IV, and as in the case of the Young's modulus variation, there is a homogeneous region but at opposite ends (right-hand side in Fig. 6(b) for the case of σ_f and left-hand side in Fig. 6(c) for the case of ε_f). In addition the overall continuous decrease of σ_f and increase of ε_f are more pronounced. It is worth mentioning that, to our knowledge, the effect of these quantities has not been studied in detail in experimental investigation of FGMs. From Fig. 6, we can see that the four FGMs under consideration present a diverse combination of spatial variation of mechanical properties (E, σ_f, and ε_f). Such a detailed knowledge of local properties will facilitate a direct correlation with fracture measurements for each FGM.

3.2. Effect of T-stress on deformation fields

The displacement field measured by the DIC technique was used to extract fracture parameters, and thus monitor crack growth resistance, for the four FGMs under consideration. As was mentioned in the introduction, it has been shown theoretically that for the case of linear elastic nonhomogeneous materials the asymptotic fields around a crack tip have the same functional form as in the case of homogeneous materials, but with material properties evaluated at the crack tip position. Therefore for the case of FGMs subjected to in-plane loading the displacement field surrounding a crack tip is given to the 2nd order by (Eischen, 1987)

$$u_x = \underbrace{\frac{K_I}{2\,G_{\text{tip}}}\left(\frac{r}{2\pi}\right)^{\frac{1}{2}}\cos\frac{\theta}{2}\left(\frac{3-v_{\text{tip}}}{1+v_{\text{tip}}}-\cos\theta\right) + \frac{2C_{12}}{G_{\text{tip}}\left(1+v_{\text{tip}}\right)}r\cos\theta}_{\text{Mode I loading}}$$
$$+ \underbrace{\frac{K_{II}}{4G_{\text{tip}}}\left(\frac{r}{2\pi}\right)^{\frac{1}{2}}\left[\frac{9+v_{\text{tip}}}{1+v_{\text{tip}}}\sin\frac{\theta}{2}+\sin\frac{3\theta}{2}\right] + \frac{2C_{22}}{G_{\text{tip}}\left(1+v_{\text{tip}}\right)}r\sin\theta}_{\text{Mode II loading}} - \underbrace{A_1 r\sin\theta + u_{0x}}_{\text{Rigid body motion}} + \text{H.O.T.}, \tag{2}$$

and

$$u_y = \underbrace{\frac{K_I}{2G_{\text{tip}}}\left(\frac{r}{2\pi}\right)^{\frac{1}{2}}\sin\frac{\theta}{2}\left(\frac{3-v_{\text{tip}}}{1+v_{\text{tip}}}-\cos\theta\right) - \frac{2C_{12}v_{\text{tip}}}{G_{\text{tip}}\left(1+v_{\text{tip}}\right)}r\sin\theta}_{\text{Mode I loading}}$$
$$+ \underbrace{\frac{K_{II}}{4G_{\text{tip}}}\left(\frac{r}{2\pi}\right)^{\frac{1}{2}}\left[\frac{5v_{\text{tip}}-3}{1+v_{\text{tip}}}\cos\frac{\theta}{2}-\cos\frac{3\theta}{2}\right] - \frac{2C_{22}}{G_{\text{tip}}\left(1+v_{\text{tip}}\right)}r\cos\theta}_{\text{Mode II loading}} + \underbrace{A_1 r\cos\theta + u_{0y}}_{\text{Rigid body motion}} + \text{H.O.T.}, \tag{3}$$

where u_x and u_y are displacement components parallel and normal to the crack plane, respectively; K_I and K_{II} are the mode I and mode II stress intensity factors, respectively; and G_{tip} and v_{tip} are the shear modulus and Poisson's ratio at the crack tip, respectively. C_{12} is a constant proportional to the nonsingular T-stress parallel to the crack plane ($T = 4C_{12}$), C_{22} is an integration constant which does not affect either the strain or the stress field, A_1 defines rigid body rotation (same effect as C_{22}), and u_{0x} and u_{0y} represent rigid body translation along the x- and y-directions, respectively. Despite the similarity of these expressions to the ones corresponding to homogeneous materials, the spatial variation of the shear modulus as the crack grows along the FGM will greatly influence the displacement field. It has been shown by Delale and Erdogan (1983) that the effect of the Poisson's ratio on K_I is almost negligible for a graded material under remote loading. For the case of homogeneous ECO, Poisson's ratio was obtained by coupling the tensile testing experiments with DIC and measuring axial and lateral strain. In both unirradiated and homogeneously

irradiated samples (50 h and 100 h) the value of Poisson's ratio was found to be 0.45. Therefore, for all FGMs value of v_{tip} was assumed constant at 0.45.

The mode I and II stress intensity factors in the FGM were obtained as a function of crack extension by fitting Eq. (3) to the raw DIC measurements, using the method of least squares as was first done in the work of McNeill et al. (1987). Displacement data used in this fit were collected only from a region *outside* 3 mm from the crack tip because of possible nonlinearity of the material within that region. As can be seen in Fig. 5 irradiated ECO shows a distinctly nonlinear behavior as strain increases, but which becomes less severe with increasing irradiation time. Since the use of Eqs. (2) and (3) requires a linear elastic material, care must be taken to use data collected from a region where nonlinear effects are not dominant. A nonlinear large deformation FEA analysis for this configuration was conducted by Li et al. (2000) who showed that nonlinear effects extend up to at most 3 mm from the tip for ECO with failure strain up to 20% and diminish with a further increase in irradiation. For this reason data used in the least squares fit of Eq. (3) were collected only beyond 3 mm from the crack tip. A confirmation of the accuracy of linear elastic fracture mechanics (LEFM) to describe the field is also obtained by evaluating the quality of the fit to the measured displacement. For larger crack extensions (greater than 50 mm) where the crack extended into less irradiated material (i.e., possessing much more than the 20% failure strain studied in Li et al. (2000)) the quality of the fit of Eq. (3) to the displacement data became poor, thus confirming the influence of nonlinear effects in the more ductile region and the inability of the LEFM field to capture them when present.

The quality of the fitting was evaluated by comparing the *measured* and *theoretical* crack tip displacement fields. The former is the result of subtracting the rigid body motion (after substituting the fitted coefficients) from the measured displacement, and the latter is the asymptotic displacement field expression using the least squares calculated coefficients. A quantitative assessment of the fitting process is given by the least squares global error. The effect of the number of terms used to fit the measured displacement, specifically the one presented in Fig. 4(d), for four different cases is shown graphically in Fig. 7 and numerically in Table 1. The dash-dotted line in Fig. 7 corresponds to experimental results, while the solid line is the theoretical prediction. Fig. 7(a) was generated from fitting only the term containing K_I (and rigid body motion), Fig. 7(b) was generated by adding the term containing K_{II}, Fig. 7(c) uses the two terms in Eq. (3) that represent pure mode I (i.e., K_I and C_{12}), and in Fig. 7(d) all six terms in Eq. (3) have been used. The value of K_{II}, although small compared to K_I, is not exactly zero. This can be attributed to camera noise and, more likely, to a small specimen-grip misalignment which was very difficult to control during the fracture tests. However, as the value of K_{II} is small compared to K_I, it is clear that the specimen failed mostly under mode I loading.

It can be seen that the best fit for the measured displacement data is obtained when all the terms on the right-hand side of Eq. (3) are used. However, Fig. 7(c) shows that it is the inclusion of the *T*-stress (through constant C_{12}) that is critical to accurately capture the displacement field. The same effect is seen when comparing the measured and theoretical strain fields. Fig. 8(a) shows a comparison between the DIC measured ε_{yy} strain component and the *K*-field (i.e., singular term only) prediction for ε_{yy} using the value of K_I obtained from the displacement field through the fit of Fig. 7(a). Fig. 8(b) shows the same comparison, but with the inclusion of the *T*-stress effect in the fitting procedure. As can be seen the effect of the *T*-stress is again pronounced and the comparison in Fig. 8(b) is better than in (a), although the experimental strain contours are much noisier than the corresponding displacement contours. (The strain contours shown are raw data, i.e., they have not been smoothed in any fashion, and this type of noise in the strain field is typical in unsmoothed DIC experimental strain data.)

From the above discussion we can conclude that both the singular K_I and nonsingular *T*-stress terms are needed to describe the fracture of the model FGMs under this mode I loading configuration. It is worth mentioning here that the *T*-stresses measured for every crack extension in all the four FGM samples were compressive, which has been (numerically) suggested to be responsible for preventing crack kinking in FGMs (Becker et al., 2001; Kim and Paulino, 2003). Fig. 9 shows the effect of the *T*-stress on the measured values of the stress intensity factor K_I for FGM III as a function of crack extension. It can be concluded
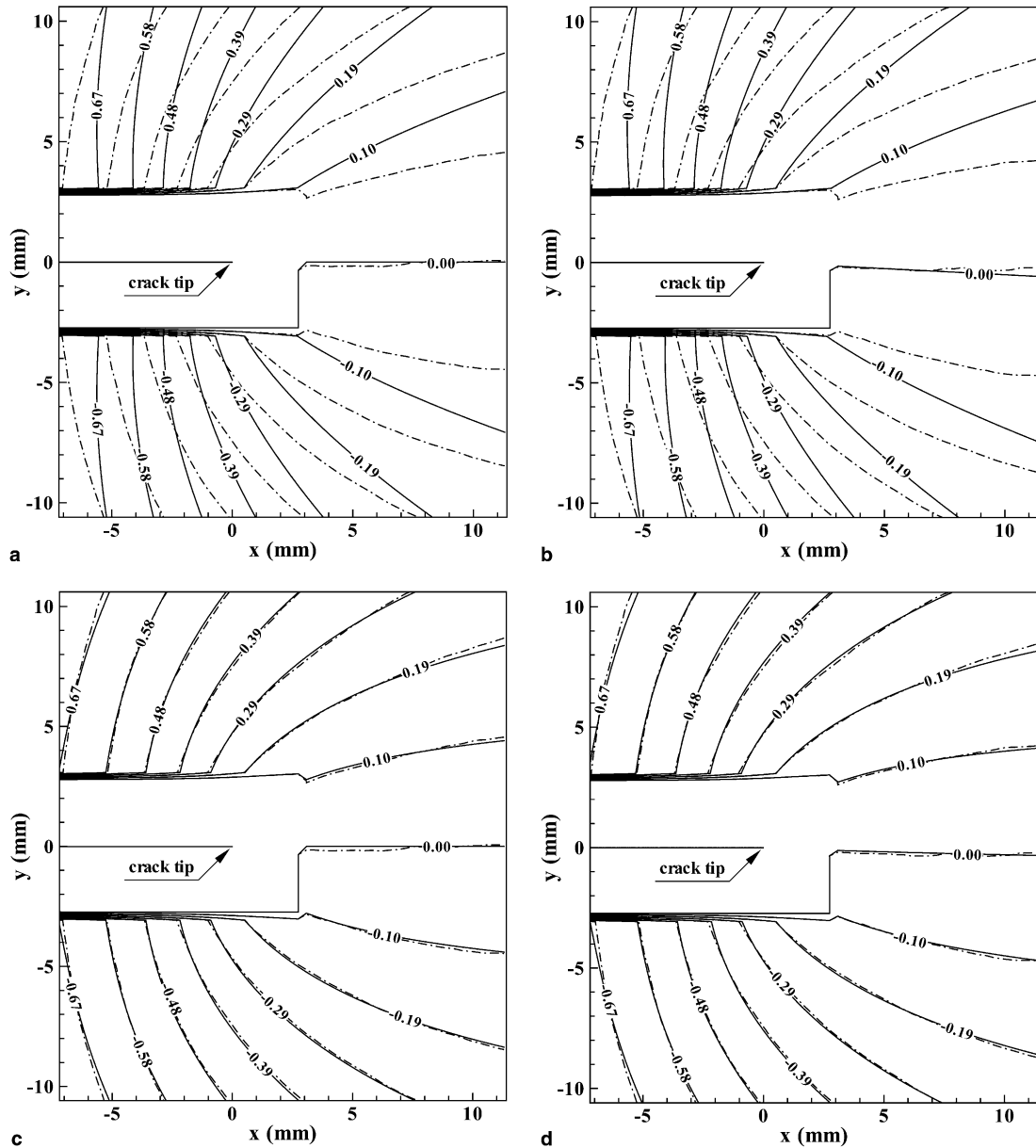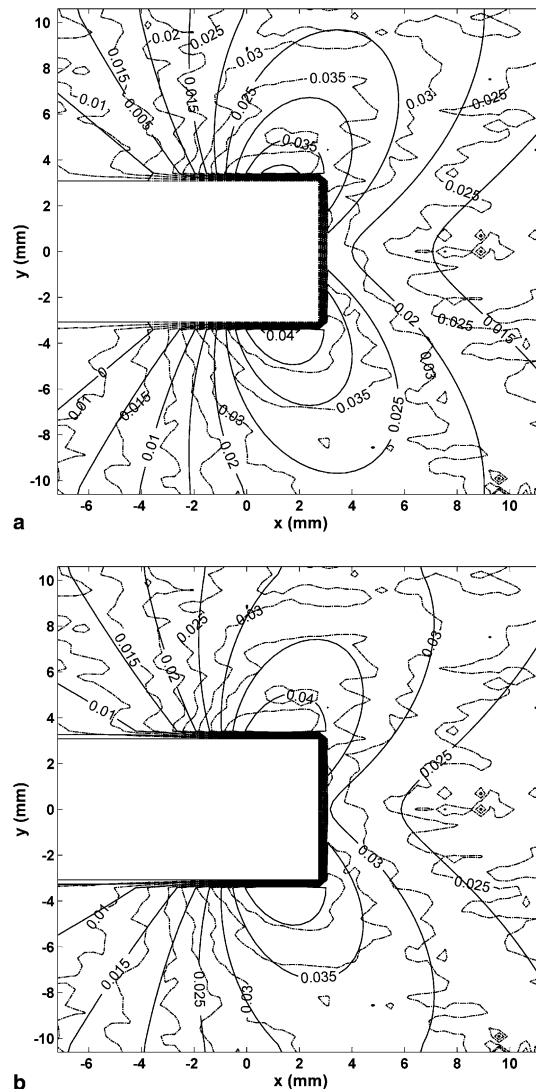
Fig. 7. Contour plots comparing *measured* (dash-dotted line) and *theoretical* (solid line) crack tip normal displacement fields as a function of the terms used to fit the displacement data presented in Fig. 4(d) The terms used in the fitting, in addition to the two terms defining rigid body motion, were (a) K_I term, (b) K_I and K_{II} terms, (c) K_I and C_{12} terms, and (d) K_I, K_{II}, C_{12}, and C_{22} terms. Notice that only data measured outside of a 3 mm region around the crack was used in the fitting as suggested by Li et al. (2000).

that assuming $T = 0$, causes an overestimation in the actual value of the mode I stress intensity factor and thus in the fracture resistance of the FGM, although the percent error decreases slightly as the crack propagates toward the more compliant region. K_{II} for the case of $T = 0$ is similar to that of the case of $T \neq 0$ and therefore is not shown in Fig. 9.

Table 1
Coefficients for four different fitting trials shown in Fig. 7

	K_I (MPam$^{0.5}$)	K_{II} (MPam$^{0.5}$)	C_{12} (MPa)	C_{22} (MPa)	A_1 (rad)	u_{0y} (mm)	Error[a] (mm^2)
Fig. 6(a)	1.612	N/A[b]	N/A[b]	N/A[b]	9.24E−4	1.309	5.727
Fig. 6(b)	1.612	−0.0414	N/A[b]	N/A[b]	3.44E−4	1.309	5.724
Fig. 6(c)	1.334	N/A[b]	−1.776	N/A[b]	9.24E−4	1.309	3.86E−2
Fig. 6(d)	1.334	−0.0414	−1.776	−4.9E−6	3.44E−4	1.309	3.62E−2

[a] Global error determined from the fitting process.
[b] Term not used in the fitting process.

Fig. 8. Contour plots comparing *measured* (dash-dotted line) and *theoretical* (solid line) ε_{yy} strain component for the DIC data presented in Fig. 7. (a) K-field only, and S (b) K_I, K_{II}, C_{12}, and C_{22} terms, used in the fitting.

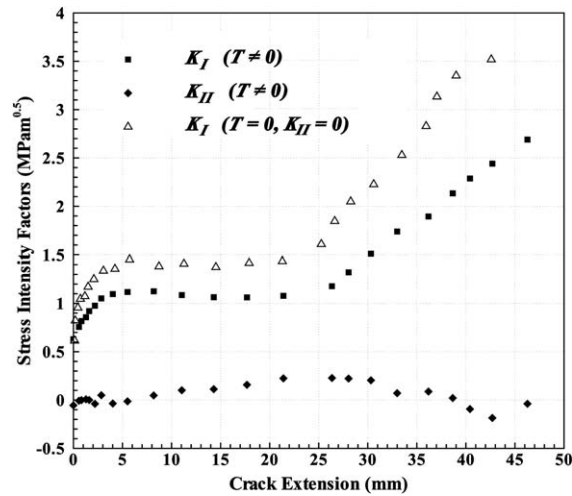Fig. 9. *T*-stress influence on the measurement of stress intensity factor K_I in FGMs.

The influence of *T*-stress on the measurement of K_I is also illustrated in Fig. 10 which shows the ratio of K_I calculated when including the *T*-stress to K_I when *T*-stress is assumed zero, plotted against crack extension for all four FGMs. As can be seen for all four material gradients tested the effect of *T*-stress on the value of K_I is at most up to about 35% and increases with increasing crack length. In Chao et al. (2001) it has been shown that in brittle *homogeneous* materials the influence of *T*-stress on the value of K_I is up to about 30% for different geometric configurations comparable to the values seen here. For the case of the FGM, however, we would like to resolve whether this influence is driven primarily from geometric effects, as in the case of homogeneous materials, or is also related to material gradient. Therefore in addition to the results for the four FGMs, Fig. 10 also shows the corresponding result for a 130 h homogeneously irradiated ECO SENT fracture experiment. The results for homogeneous ECO follow the same decreasing
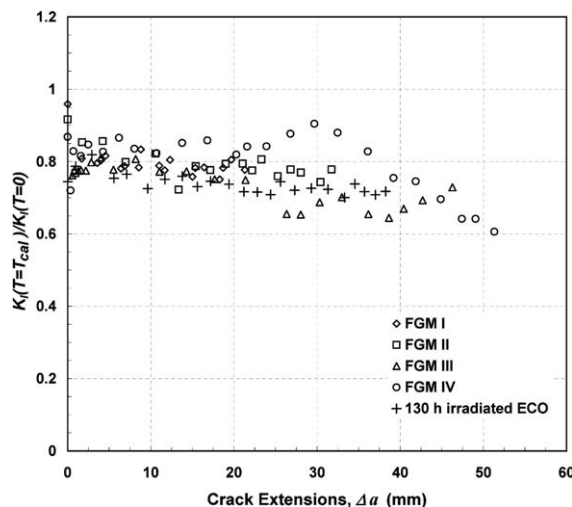

Fig. 10. Effect of *T*-stress on the mode I stress intensity factor for the four FGM samples illustrated through the ratio of K_I obtained when *T*-stress is taken into account divided by K_I when *T*-stress is assumed to be 0. For comparison results from a 130 h homogeneously irradiated sample are also shown.

trend with increasing crack length and the influence of *T*-stress on K_I is also of same order although it does not exceed 30%, which is in agreement with the result of Chao et al. (2001). The larger influence of *T*-stress on K_I occurs for FGMs III and IV which are the samples with the steeper material property gradient. Therefore these results imply that the influence of *T*-stress on K_I is primarily a geometric effect, and the influence of material gradient, although possible for large property gradients, is a second order effect.

3.3. Crack growth resistance

Crack growth resistance was monitored by plotting K_I as a function of crack extension, Δa, for the four FGMs. The results, along with the corresponding spatial variation of Young's modulus, failure stress and failure strain, are shown in Figs. 11–14.
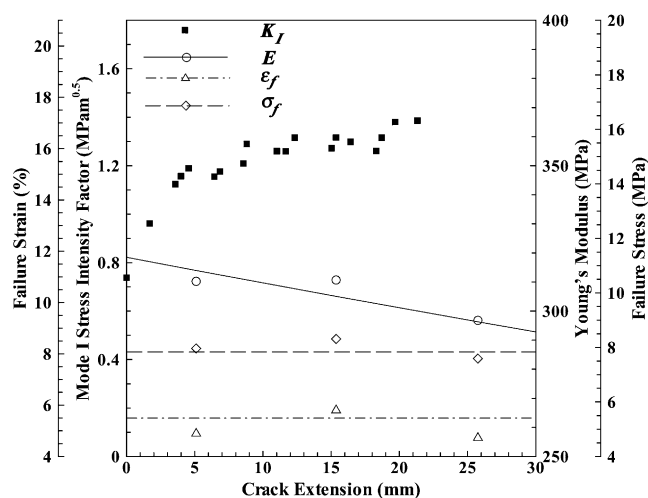

Fig. 11. Resistance curve for FGM I, also showing the corresponding spatial variation of *E*, σ_f and ε_f.
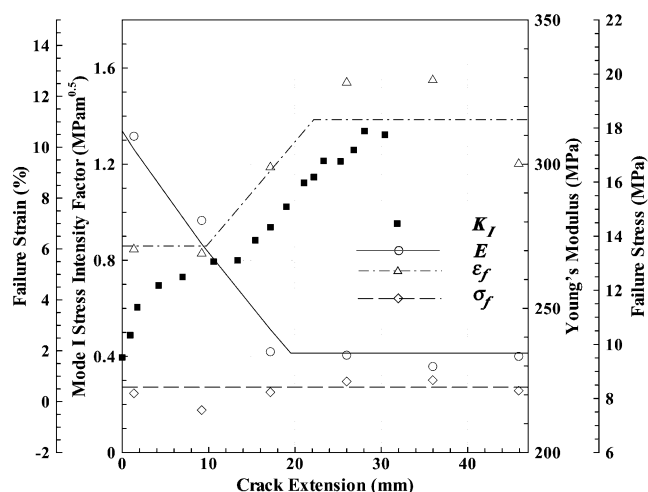

Fig. 12. Resistance curve for FGM II, also showing the corresponding spatial variation of *E*, σ_f and ε_f.
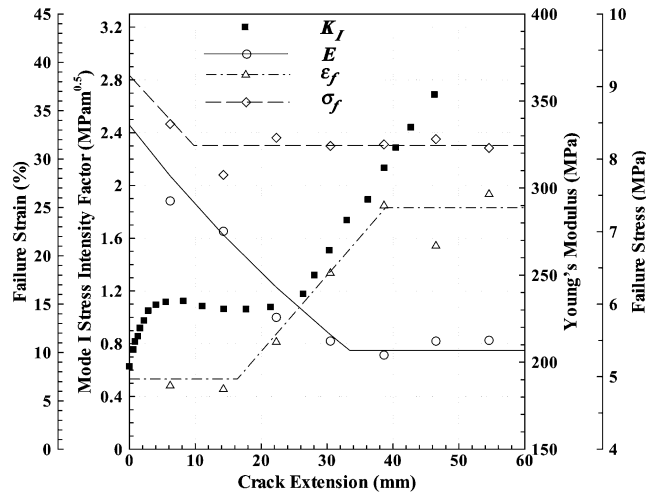
Fig. 13. Resistance curve for FGM III, also showing the corresponding spatial variation of E, σ_f and ε_f.
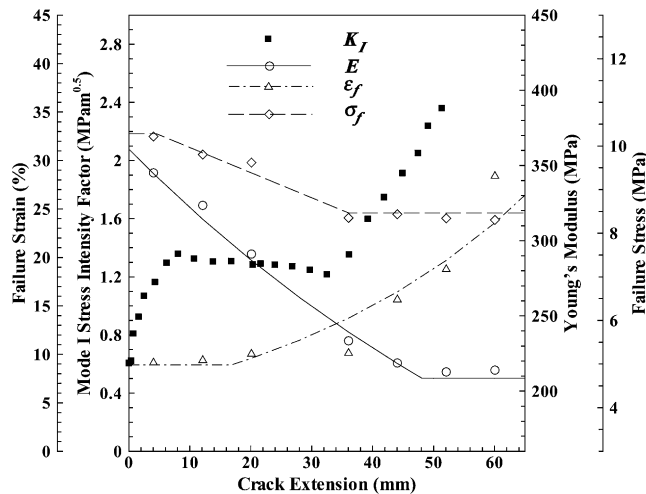

Fig. 14. Resistance curve for FGM IV, also showing the corresponding spatial variation of E, σ_f and ε_f.

Fig. 11, for FGM I, shows a resistance curve that rises rapidly for small crack extensions ($\Delta a < 5$ mm), but as the crack keeps growing, reaches a plateau and does not exhibit any "built-in" toughening (Erdogan, 1995). This is in contrast to the results of Li et al. (2000) that measured a constantly increasing resistance curve for their FGM. By examining the variation of E, σ_f and ε_f as the crack grows through the graded material, we can see that although E decreases, ε_f and σ_f remain almost invariant. However, the variation of Young's modulus along the entire FGM I sample is relatively mild and specifically in the window of crack growth of 30 mm shown in Fig. 11 varies only by about 8.5% or about 1 MPa/mm. One of the advantages of the UV irradiation technique used to generate the FGMs is that the variation of properties can be controlled, within the limitations of the material, by the duration and amount of irradiation, and FGMs II, III and IV were manufactured to have steeper modulus gradient in the vicinity of the initial crack tip. The effect of modulus hinted to in Fig. 11 is seen more clearly in the early stages of crack growth in FGMs II

and III, Figs. 12 and 13, where up to a crack extension of about 14 mm and 20 mm respectively there is little change in the failure stress and strain compared to a Young's modulus decrease of 20% (or 3.7 MPa/mm) and 43% (or 5 MPa/mm) respectively. The fact that in FGMs II and III the crack again reaches steady state growth where the fracture resistance remains constant, much like in the case of homogeneous materials, implies that the spatial variation of E does not affect the overall fracture resistance of the FGM. However, the Young's modulus variation does affect the stress distribution around the crack tip, illustrated through Eq. (3), and therefore the applied load needed for continued crack growth. This was also observed by Neubrand et al. (2003).

The corresponding curve for FGM II is shown in Fig. 12. In this case the original crack tip was placed in a region where σ_f and ε_f are almost constant while E shows a sharper gradient. Compared to FGM I, this resistance curve clearly illustrates the effect of E and ε_f on the fracture response. The FGM II property variation can be divided into three regions: (i) Decreasing E and constant ε_f, up to approximately 12 mm of crack extension. As mentioned above, the situation in this range is similar to that in FGM I (Fig. 11), and crack growth resistance almost reaches a plateau even though E decreases. (ii) In the second region (about 10 mm $< \Delta a <$ 25 mm) ε_f increases and as a consequence the FGM fracture resistance also increases, showing that it is highly controlled by local failure strain. The Young's modulus will affect the available driving force through the stress field, therefore the measured driving force must increase to allow crack growth *in spite of the decreasing* Young's modulus. (iii) In the third region ($\Delta a >$ 25 mm), ε_f and E reach constant values; however measured values of ε_f show a much larger deviation from the fitted line compared to the two previous regions. In this region, it seems that the curve eventually reaches a constant value. However, data for larger crack extensions would be needed to determine if a plateau is really achieved following the trend of ε_f. Nonetheless, the results of the two first regions are quite significant confirming that the overall fracture resistance of the FGM follows the spatial variation of ε_f (with almost constant σ_f in this case).

The regions of (i) constant E and ε_f (up to about 20 mm), and (ii) decreasing E and increasing ε_f, with an approximately constant σ_f are also seen to occur in FGM III (Fig. 13). Here, as in FGMs I and II, crack growth resistance reaches a steady state plateau in the initial stages of growth which is followed by an increase resulting from a large increase in the local failure strain. In all three cases of FGMs I, II and III, however, it is difficult to draw conclusions regarding the influence of failure stress on crack growth resistance as it varies little in these samples. For this purpose FGM IV was manufactured to exhibit a larger variation of local failure stress in the window of interest. Fig. 14 shows the fracture resistance curve of FGM IV and the corresponding spatial variation of E, σ_f and ε_f. From this Figure we can clearly see that, in addition to ε_f, σ_f does also directly affect the fracture resistance of the FGM. In this case the FGM fracture resistance initially decreases as does σ_f. A decreasing resistance curve in homogeneous materials is considered an unstable state where the applied driving force has reached a critical value equal to the fracture toughness of the materials (which is constant), and increasing the driving force above this critical value will cause a sudden and catastrophic material failure. However this may or may not happen in the case of functionally graded materials depending on the combination of local values of σ_f and ε_f. For example in the case of FGM IV, initially fracture resistance is controlled by σ_f as ε_f remains constant. Then the crack propagates through a region where σ_f decreases while ε_f increases, in this case the combined effect of both will determine the fracture toughness of the FGMs. A third case occurs when ε_f increases and σ_f is constant, in this case the toughness of the material is controlled solely by ε_f. Therefore, in contrast to the fracture toughness of homogeneous materials which depends only on the crack extension, the fracture resistance of functionally graded materials will depend, in addition to the crack extension, on the combined effect of the local values of σ_f and ε_f.

Based on the previous discussion, we can now rewrite Eq. (1) for the case of graded materials to formulate a fracture criterion for quasi-static crack propagation in FGMs under small scale yielding mode I loading as

$$K_I(P, a, E(x), T) = K_I^R(\Delta a, \varepsilon_f(x), \sigma_f(x)). \qquad (4)$$

The available stress intensity factor K_I appearing on the left hand side will depend on loading (P) and geometry (a), as in the case of homogeneous materials, but also on the local elastic modulus ($E(x)$, x: gradient direction) and T-stress (T). Crack growth will occur when this driving force equals a toughness, K_I^R, a material property, which will depend not only on crack extension (Δa) as in homogeneous materials, but also the local failure strain, $\varepsilon_f(x)$, and failure stress, $\sigma_f(x)$. Note that since small scale yielding conditions have been assumed Eq. (4) can also be recast in a form involving energy release rate.

4. Conclusions

The aim of this experimental investigation was to provide a broader understanding of the parameters that control the fracture behavior of functionally graded materials. To achieve this goal, model polymer-based graded materials were manufactured and mechanically characterized in detail using uniaxial tensile tests. Their in-plane fracture behavior was also investigated using the full-field digital image correlation (DIC) technique. This is the first time that experiments of this kind have been conducted on polymer-based FGMs. The very detailed characterization of each specimen coupled with full-field optical diagnostics allowed a comprehensive analysis of the role of all relevant parameters.

A fracture criterion for functionally graded materials was suggested in which crack growth occurs when the (applied) crack driving force reaches a critical value equal to the FGM fracture toughness. It was shown experimentally that in FGMs, the crack driving force depends on the local values of the Young's modulus and the corresponding T-stress. The fracture toughness of FGMs, in contrast to homogeneous materials, exhibits a spatial variation that directly depends, in addition to the crack extension (as in homogeneous materials), on the combined effect of two local material parameters: failure stress σ_f and failure strain ε_f. Depending on the spatial variation of these two parameters, the local FGM fracture toughness will possess, regardless the spatial variation of the Young's modulus, a constant value (when σ_f and ε_f are constant), increasing behavior (when σ_f and/or ε_f locally increase), or decreasing behavior (when σ_f and/or ε_f locally decrease).

A logical continuation of this work is to investigate the precise details of how σ_f and ε_f affect the right-hand side of expression (4). The particular material used here, ECO, fails through a process of crazing which, even though not visible at the scale of the image in Fig. 4(b), can readily be visualized in an optical microscope. Abanto-Bueno and Lambros (2005) have directly measured craze level properties and related them to global toughness values for homogeneously irradiated ECO. A companion study for graded ECO is currently underway which should shed more light into the exact dependence of K_I^R on $\sigma_f(x)$ and $\varepsilon_f(x)$.

References

Abanto-Bueno, J., Lambros, J., 2004. Mechanical and fracture behavior of an artificially ultraviolet-irradiated poly(ethylene carbon monoxide) copolymer. Journal of Applied Polymer Science 92 (1), 139–148.

Abanto-Bueno, J., Lambros, J., 2005. Experimental determination of cohesive failure properties of a photo-degradable copolymer. Experimental Mechanics 45 (2).

Abanto-Bueno, J., Lambros, J., 2002. Investigation of crack growth in functionally graded materials using digital image correlation. Engineering Fracture Mechanics 69 (14–16), 1695–1711.

Anderson, T.L., 1995. Fracture Mechanics: Fundamentals and Applications. CRC Press LLC, Florida.

Andrady, A.L., 1990. Weathering of polyethylene (LPDE) and enhanced photodegradable polyethylene in the marine environment. Journal of Applied Polymer Science 39 (2), 363–370.

Andrady, A.L., Pegram, J.E., Nakatsuka, S., 1993. Studies on enhanced degradable plastics: 1. The geographic variability in outdoor lifetimes of enhanced photodegradable polyethylenes. Journal of Environmental Polymer Degradation 1 (1), 31–43.

Anlas, G., Santare, M.H., Lambros, J., 2000. Numerical calculation of stress intensity factors in functionally graded materials. International Journal of Fracture 104 (2), 131–143.

Becker Jr., T.L., Cannon, R.M., Ritchie, R.O., 2001. Finite crack kinking and *T*-stresses in functionally graded materials. International Journal of Solids and Structures 38 (32–33), 5545–5563.

Bruck, H.A., McNeill, S.R., Sutton, M.A., Peters III, W.H., 1989. Digital image correlation using Newton–Raphson method of partial-differential correction. Experimental Mechanics 29 (3), 261–267.

Butcher, R.J., Rousseau, C.E., Tippur, H.V., 1999. A functionally graded particulate composite: preparation, measurements and failure analysis. Acta Materialia 47 (1), 259–268.

Chalivendra, V.B., Shukla, A., Parameswaran, V., 2003. Quasi-static stress fields for a crack inclined to the property gradation in functionally graded materials. Acta Mechanica 162 (1–4), 167–184.

Chao, Y.J., Liu, S., Broviak, B.J., 2001. Brittle fracture: variation of fracture toughness with constraint and crack curving under mode I conditions. Experimental Mechanics 41 (3), 232–241.

Cichocki, F.R., Trumble, K.P., Rödel, J., 1998. Tailored porosity gradients via colloidal infiltration of compression-molded sponges. Journal of the American Ceramic Society 81 (6), 1661–1664.

Chin, E.S.C., 1999. Army focused research team on functionally graded armor composites. Materials Science and Engineering A 259 (2), 155–161.

Delale, F., Erdogan, F., 1983. The crack problem for a non-homogeneous plane. Journal of Applied Mechanics-Transactions of the ASME 50 (3), 609–614.

Eischen, J.W., 1987. Fracture of nonhomogeneous materials. International Journal of Fracture 34 (1), 3–22.

Erdogan, F., 1995. Fracture mechanics of functionally graded materials. Composites Engineering 5 (7), 753–770.

Erdogan, F., Wu, B.H., 1997. The surface crack problem for a plate with functionally graded properties. Journal of Applied Mechanics-Transactions of the ASME 64 (3), 449–456.

Gasik, M.M., Ueda, S., 1999. Micromechanical modeling of functionally graded W–Cu materials for divertor plate components in a fusion reactor. Materials Science Forum 308–311, 603–607.

Ivanova, E., Chudnovsky, A., Wu, S., Sehanobish, K., Bosnyak, C.P., Wu, S., 1996. A new experimental technique for modeling of a micro-heterogeneous media. Experimental Techniques 20 (6), 11–13.

Jin, Z.-H., Batra, R.C., 1996. Some basic fracture mechanics concepts in functionally graded materials. Journal of the Mechanics and Physics of Solids 44 (8), 1221–1235.

Kim, J.-H., Paulino, G.H., 2003. *T*-stress, mixed mode stress intensity factors, and crack initiation angles in functionally graded materials: a unified approach using the Interaction Integral Method. Computer Methods in Applied Mechanics and Engineering 192 (11–12), 1463–1494.

Konda, N., Erdogan, F., 1994. The mixed mode crack problem in a nonhomogeneous elastic medium. Engineering Fracture Mechanics 47 (4), 533–545.

Kubair, D.V., Geubelle, P.H., Lambros, J., in press. Asymptotic analysis of a mode 3 stationary crack in a ductile functionally graded material. Journal of Applied Mechanics.

Lambros, J., Santare, M.H., Li, H., Sapna III, G.H., 1999. A novel technique for the fabrication of laboratory scale model functionally graded materials. Experimental Mechanics 39 (3), 184–190.

Li, H., Lambros, J., Cheeseman, B.A., Santare, M.H., 2000. Experimental investigation of the quasi-static fracture of functionally graded materials. International Journal of Solids and Structures 37 (27), 3715–3732.

McNeill, S.R., Peters, W.H., Sutton, M.A., 1987. Estimation of stress intensity factor by digital image correlation. Engineering Fracture Mechanics 28 (6), 101–112.

Neubrand, A., Chung, T.J., Rödel, J., 2003. Experimental and theoretical investigation of *R*-curve behaviour in Al/Al2O3 functionally graded materials. Materials Science Forum 423–4, 269–274.

Niino, M., Maeda, S., 1990. Recent development status of functionally gradient materials. ISIJ International 30 (9), 699–703.

Parameswaran, V., Shukla, A., 2002. Asymptotic stress fields for stationary cracks along the gradient in functionally graded materials. Journal of Applied Mechanics-Transactions of the ASME 69 (3), 240–243.

Pompe, W., Worch, H., Epple, M., Friess, W., Gelinsky, M., Greil, P., Hempel, U., Scharnweber, D., Schulte, K., 2003. Functionally graded materials for biomedical applications. Materials Science and Engineering A 362 (1–2), 40–60.

Rousseau, C.-E., Tippur, H.V., 2000. Compositionally graded materials with cracks normal to the elastic gradient. Acta Materialia 48 (16), 4021–4033.

Sutton, M.A., Wolters, W.J., Peters, W.H., Ranson, W.F., McNeill, S.R., 1983. Determination of displacements using an improved digital image correlation method. Image and Vision Computing 1 (3), 133–139.

Vendroux, G., Knauss, W.G., 1998. Submicron deformation field measurements: Part 2. Improved digital image correlation. Experimental Mechanics 38 (2), 86–92.

Watari, F., Yokoyama, A., Matsuno, H., Saso, F., Uo, M., Kawasaki, T., 1999. Biocompatibility of titanium/hydroxyapatite and titanium/cobalt functionally graded implants. Materials Science Forum 308–311, 356–361.

Yamada, K., Sakamura, J., Nakamura, K., 1999. Broadband ultrasound transducers using piezoelectrically graded materials. Materials Science Forum 308–311, 527–532.

Zhao, J., Ai, X., Huang, X.P., 2002. Relationship between the thermal shock behavior and the cutting performance of a functionally graded ceramic tool. Journal of Materials Processing Technology 129 (1–3), 161–166.